STUDIA UBB CHEMIA, LX, 3, 2015 (p. 31-52)
(RECOMMENDED CITATION)

Dedicated to prof. dr. I. C. Popescu
on the occasion of his 70th anniversary

GRAPHENE AND CARBON NANOTUBE NANOMATERIALS IN LAYER-BY-LAYER STRUCTURED ELECTROCHEMICAL ENZYMATIC BIOSENSORS: A REVIEW

MADALINA M. BARSAN, CHRISTOPHER M.A. BRETT[a*]

ABSTRACT. This review highlights the recent developments made, during the past five years, from 2010 onwards, in biosensors that bring together the advantages of the layer-by-layer (LbL) methodology and the use of graphene and carbon nanotubes as carbon nanomaterials. LbL methodology in biosensor assembly has been widely used to incorporate suitable materials with controlled molecular architecture, enabling the build-up of stable and complex architectures. At the same time, the incorporation of nano-sized materials into a sensing device has been exploited in order to improve the electronic communication between the enzyme and the electrode substrate. The advantages of incorporating carbon nanomaterials (CN) into LbL multilayers for the development of biosensors with improved analytical performance are described. The key steps for the incorporation of CN in self assembled architectures are the choice of the type of CN functionalization and pairing with an adequate oppositely-charged polyelectrolyte. The preparation of the LbL assembly will be described in detail. Electrochemical and surface characterization will underline the importance of incorporating CN and identify their nanostructures and build-up in the LbL assembly. Finally, applications of CN-LbL biosensors will exemplify their utility as analytical tools for the detection of key analytes, such as glucose, ethanol, cholesterol and neurotoxins.

Keywords: *carbon nanomaterials, graphene, carbon nanotubes, layer by layer, self-assembly, enzyme biosensors*.

[a] *Department of Chemistry, Faculty of Sciences and Technology, University of Coimbra, 3004-535 Coimbra, Portugal*
[*] *Corresponding author: cbrett@ci.uc.pt*

1. INTRODUCTION

Electrochemical enzyme biosensors can have a wide range of applications in the clinical and diagnostic field, environmental, agricultural and food industry. The key to produce effective biosensors is to immobilize the enzyme in such a way as to maintain their bio-functionality, at the same time providing accessibility toward the target analyte and an intimate contact with the electrode substrate. The assembly of suitable materials with controlled molecular architecture in multicomponent thin films can be carried out by techniques such as physical immobilization, through weak bonds such as Van der Waal's forces, by electrostatic and/or hydrophobic interactions. Such configurations offer both a good preservation of enzyme activity [1] and the possibility of direct electron transfer between enzyme and electrode [2]. Since enzymes are natural polyelectrolytes, their alternate deposition together with tailored oppositely charged species in layer-by-layer structures onto solid substrates, has been widely used to develop LbL biosensors [3, 4]. The deposition of more bilayers implies immobilization of more enzyme through the LBL procedure, but a thicker multilayer film may also lead to an increase in the electron transfer resistance and a decrease in enzyme substrate diffusion [5]. In order to improve electronic communication between the enzyme and the electrode substrate, the incorporation of nano-sized materials into a sensing device has been extensively investigated. Among nano-sized materials, carbon-based ones are those most employed for the construction of new and improved biosensor architectures, due, particularly, to their good biocompatibility and relatively low cost. Both graphene (G) and carbon nanotubes (CNT) exhibit excellent thermal conductivity, mechanical properties and extraordinary electronic transport properties [6]. The large surface area and excellent electrical conductivity allow them to act as an ''electron wire'' between the redox centres of an enzyme or protein and an electrode surface, leading to their wide use as electrocatalysts in a large variety of biosensor constructions [7-9]. The functionalization of carbon nanomaterials is a critical step, prior to their use, being required for their solubilisation by dispersion, purification and further processing and applications [10]. In the case of graphene, functionalization is required for its application in sensors, since pristine graphene is a zero band gap, inert material [11, 12]. For their use in layer-by-layer assemblies based on electrostatic interactions, CN can be functionalized so as to possess either positively- or negatively-charged surfaces [8, 13].

The present review highlights the important developments during the last 5 years in biosensors that make use of the advantages of both carbon nanomaterials and LbL methodology. Different strategies for preparing the

self-assembled multilayered structures are discussed, based mainly on electrostatic attraction, but also on other interactions such as hydrogen bonding, π-π interaction, sequential covalent reactions. It will stress the functionalization of the carbon nanomaterials and the species used to enable their incorporation in LbL structures, such as metal nanoparticles, polyelectrolytes, and polymers, including dendrimers. The chemical structure of the most used charged polymers is given in Fig. 1.

Electrochemical and surface characterization of the LbL structures will be discussed, focusing on the monitoring of the multilayer deposition and on the electronic conductivity of the final assembly.

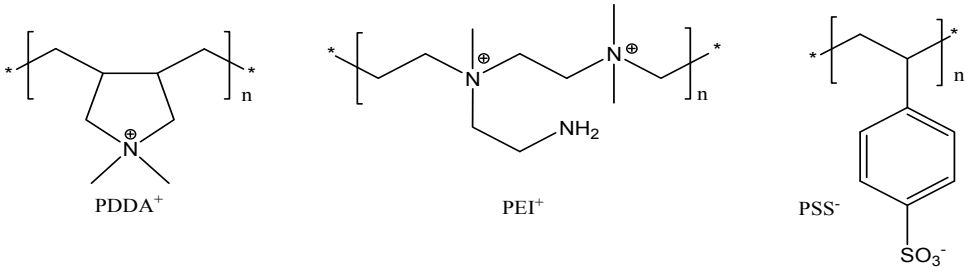

Figure 1. Chemical structures of commonly used charged polymers in LbL: poly(dimethyldiallyammonium chloride) ($PDDA^+$), polyethylimine (PEI^+) and polystyrene sulfonate(PSS^-).

Finally, examples of biosensor application will be given, with a focus on the analytical performance of the biodevice.

2. PREPARATION

Biosensors prepared by using LbL assembly have been mainly based on electrostatic, and some on either covalent or non-covalent π-π stacking interaction or biospecific interaction. A typical LbL assembly, containing graphene or CNT is exemplified in Fig. 2.

2.1. Graphene in LbL

In order to enable the assembly of negatively-charged graphene (G) in LbL structures, several positively-charged species were used, such as the polymers poly(dimethyldiallyammonium chloride) ($PDDA^+$) [14-16] or polyethyleneimine (PEI^+) [17], amino-terminated ionic liquid [18], amino functionalized CNT [15, 16, 19], and redox compounds such as methylene green (MG) [16] and alcian blue pyridine (AB) [20]. In [21], pyrene-functionalized glucose oxidase (GOx) was assembled with graphite through π-π stacking interactions. In [22, 23], graphene was dispersed into positively-charged

chitosan together with the enzyme, and assembled in LbL by using poly(styrene sulfonate) (PSS^-). Some non-enzymatic LbL structures containing graphene were developed as substrates for enzyme immobilization, based on electrostatic interaction between bovine serum albumin (BSA^+) functionalized G and $AuNP^-$ [24], negatively-charged G and chitosan [25], one based on the π-π interaction between MB and G [26], and another based on both covalent and hydrophobic interactions between G and Prussian blue (PB) through octadecylamine linkers [27].

Multilayer films composed of Prussian blue nanoparticles (PB), graphene and GOx have been assembled on a glassy carbon electrode (GCE). Prior to LbL formation, an adsorbed positively-charged monolayer of $PDDA^+$ was first allowed to form, followed by multilayer film growth by sequential dipping of the modified electrodes into the graphene solution, into the as-prepared positively charged PDDA-PB^+, the negatively-charged GOx solution, PDDA-PB^+, then repeating these steps to form GCE/$\{G^-$/PDDA-PB^+/GOx^-/PDDA-$PB^+\}_3$ [14].

(a)

(b)

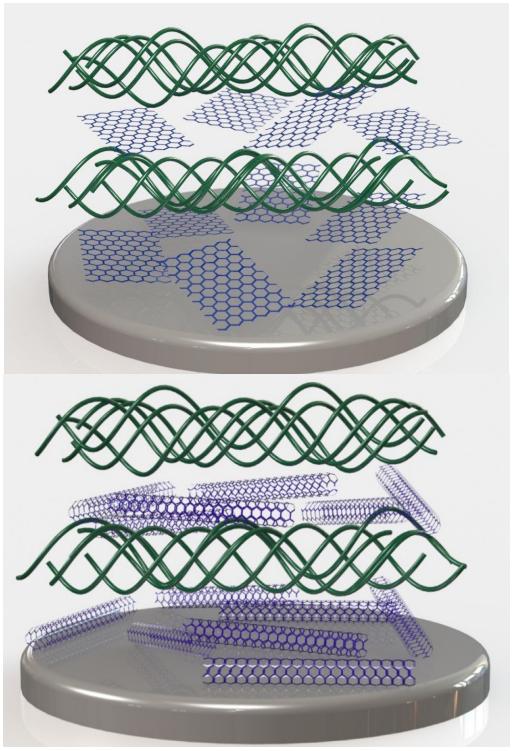

Figure 2. Schematic representation of carbon nanomaterials assembled in LbL multilayer structures of (a) graphene and (b) CNT.

A graphite electrode (GE) modified with $PDDA^+$ and polystyrenesulphonate (PSS^-) was used as substrate for the deposition of $G\text{-}COO^-$ and $CNT\text{-}NH_3^+$ to obtain $GE/PDDA^+/PSS^-\{CNT\text{-}NH_3^+/G\text{-}COO^-\}_5$, on top of which alcohol dehydrogenase (AlcDH) was immobilized by drop casting. $G\text{-}COO^-$ was obtained by treating G with concentrated HNO_3, and $CNT\text{-}NH_3^+$ was obtained by first treating CNT with H_2SO_4:HNO_3 (3:1 v/v) followed by thionyl chloride and then ethylene diamine [15].

The positively-charged species, methylene green (MG^+) and methylimidazolium-functionalized CNT, were assembled with negatively-charged graphene *via* electrostatic and/or π-π interactions to form multilayered structures of G^-/MG^+ and G^-/CNT^+. The substrate was first modified with $PDDA^+$ and then with G^- and MG^+ or CNT^+ to obtain the final modified electrode assemblies, designated as $GCE/PDDA^+/\{G^-/MG^+\}_5$ and $GCE/PDDA^+/\{G^-/CNT^+\}_5$. The enzymes AlcDH and glucose dehydrogenase (GDH) were immobilized on top by cross-linking with glutaraldehyde [16].

Modification with PEI^+ and poly(acrylic acid)$^-$-G (PAA^--G) multilayer films on GCE was performed by alternately immersing the electrode in PEI^+ solution and in PAA^--G solution. The $GCE/\{PEI^+/PAA^-\text{-}G\}_n$ was used as substrate for the deposition of the enzyme, in a similar manner, using negatively charged GOx^- or glucoamylase (GA^-) enzyme solutions and PEI^+ to obtain the biosensors $GCE/\{PEI^+/PAA^-\text{-}G\}_3/\{PEI^+/GOx^-\}_5$ and $GCE/\{PEI^+/PAA^-\text{-}G\}_3/\{PEI^+/GOx^-\}_5/\{PEI^+/GA^-\}_4$ [17].

Amine-terminated ionic liquid ($G\text{-}IL\text{-}NH_3^+$), and sulfonic acid functionalized graphene ($G\text{-}SO_3^-$) were self-assembled by covalent bonding. GOx adhered to $G\text{-}IL\text{-}NH_3^+$, after immersing the electrode in GOx in solution, the biosensor being finally coated with Nafion to obtain $GCE/\{G\text{-}IL\text{-}NH_3^+/G\text{-}SO_3^-\}/G\text{-}IL\text{-}NH_3^+/GOx^-$/Nafion [18].

Positively-charged $CNT\text{-}NH_3^+$ and negatively charged $G/TiO_2\text{–}Pd^-$ hybrid were assembled on a GCE. Negatively-charged GOx^- was then adsorbed on $CNT\text{-}NH_3^+$ and was finally covered with Nafion to obtain $GCE/\{CNT\text{-}NH_3^+/G\text{-}TiO_2\text{-}Pd^-\}_9/CNT\text{-}NH_3^+/GOx^-$/Nafion [19].

For the deposition of LbL layers of positively- and negatively-functionalized G, first a negatively-charged layer was formed on GCE by electrochemical potential cycling modification with sulfanilic acid (ABS^-). Graphene composites functionalized with copper phthalocyanine-3,4,4,4-tetrasulfonic acid tetrasodium salt ($G\text{-}TSCuPc^-$) or its alcian blue pyridine variant ($G\text{-}AB^+$) were assembled via alternate electrostatic adsorption onto the GCE/ABS^- surface to form $GCE/ABS^-/\{G\text{-}AB^+/G\text{-}TSCuPc^-\}_3/G\text{-}AB^+$. GOx solution in Nafion was afterwards dropped onto the LbL modified electrode to obtain the biosensor [20].

In another procedure, GOx was first modified with pyrene functionalities in order to be self-assembled onto graphene basal plane *via* π-π stacking interactions to obtain GCE/{G/GOx-pyrene}$_3$ [21].

In [22, 23], carbon nanomaterials (CN), nitrogen doped graphene (NG) and HNO_3 and KOH functionalized G and CNT were dispersed together with the enzyme GOx in the positively-charged polymer chitosan. LbL assembly was carried out together with the negatively charged PSS^-, to finally obtain {chit$^+$(CN+GOx)/PSS^-}$_n$ structures on gold electrodes. When the CN was NG the best biosensor contained 2 bilayers whereas when the CN was HNO_3 or KOH functionalized G (and CNT), the optimum biosensor was based on 4 bilayers.

Four types of LbL modified electrodes were reported for use as supports for posterior enzyme immobilization [24-27]. Negatively-charged $AuNP^-$ have been assembled in multilayers with BSA functionalized G (BSA-G$^+$) on fluorine doped tin oxide (FTO) electrodes previously modified with PEI$^+$. To improve the conductivity of the modified electrode, thermal annealing was introduced in order to decompose BSA on the surface of the graphene nanosheets [24]. Multilayer films of positively-charged chitosan and negatively-charged G were assembled on GCE to obtain GCE{chit$^+$/G$^-$}$_5$ [25]. The electroactive dye methylene blue (MB) was adsorbed onto G through π-π stacking and hydrophobic interactions and assembled on GCE to form GCE/{G/MB}$_n$ [26]. Finally, films of graphene oxide (GO)-Prussian blue (PB) hybrids were deposited on graphite screen-printed electrodes (GrSPE) using octadecylamine (ODA), acting as a bifunctional linker between GrSPE and the GO and as an anchoring layer for the immobilization of the PB through hydrophobic interactions. Before immobilizing PB, GO was chemically reduced in $NaBH_4$ solution [27].

2.2. CNT in LbL

For the assembly of negatively-charged CNT into multilayer films, different cationic polymers were used: PEI$^+$ [28], poly[(vinylpyridine) Os(bipyridyl)$_2$Cl] (PVI-Os$^+$) [29, 30], poly(amido amine) (PAMAM$^+$) [31, 32], poly(allylamine hydrochloride) (PAH) [33], and thionine$^+$ [34]. Positively-charged CNT were also used in LbL assemblies and were obtained by functionalization with PDDA$^+$ [35] or PEI$^+$ [36, 37], and enabled direct adsorption of negatively-charged enzymes. In [38], negatively-charged CNT were co-immobilized with PtNP.

In [28], CNT^- were immobilized together with GOx^- alternately with PEI$^+$, to obtain GCE/CNT^-/{PEI$^+$/GOx^-}$_3$/PEI$^+$ [28].

Cationic PVI-Os$^+$ was also used to enable the incorporation of GOx and CNT in multilayer structures deposited on screen printed carbon electrodes (SPCE). First, the polymer was electrodeposited to obtain a positively-charged substrate, GCE/PVI-Os$^+_{el}$, followed by alternate deposition of GOx-CNT conjugate and cationic PVI-Os from their respective solutions. As last step, PVI-Os

was again electrodeposited on top to stabilize the multilayer structures and the final biosensor was SPCE/PVI-Os^{+}_{el}/{GOx-CNT^{-}/PVI-Os^{+}}$_4$/PVI-Os_{el}^{+} [29]. A similar approach was used by the same authors, but instead of CNT-GOx conjugates, using CNT and GOx separately, in order to obtain SPCE/{PVI-Os^{+}_{el}/ CNT^{-}/PVI-Os_{el}/ GOx^{-}}$_5$/PVI-Os_{el} [30].

PAMAM dendrimer-encapsulated platinum nanoparticles (PtNP-$PAMAM^{+}$) were used to immobilize negatively-charged GOx^{-}. PtNP-$PAMAM^{+}$ were linked to CNT, previously dropped on the ITO, with 1-ethyl-3-[3 -(dimethylamino)propyl] carbodiimide (EDC), to obtain GCE/CNT^{-}/PtNP-$PAMAM^{+}$ which served as anchor for the negatively-charged GOx, and the steps repeated to form ITO/CNT^{-}/{PtNP-$PAMAM^{+}$/GOx^{-}}$_3$ [31].

A bienzyme biosensor prepared for the detection of cholesterol was based on CNT mixed with gold nanoparticles (AuNP) wrapped with cationic poly(allylamine hydrochloride) (PAH). An Au electrode was first immersed in mercaptopropansulfonate (MPS) to form Au-MPS^{-}, followed by deposition of the polycation PAH^{+} and then the polyanion PSS^{-}. Au/MPS^{-}/PAH^{+}/PSS^{-} was then modified by LbL assembly of {PAH-CNT-$AuNP^{+}$/HRP^{-}}$_n$ and {PAH-CNT-$AuNP^{+}$/ $ChOx^{-}$}$_n$ were deposited on top to obtain Au/MPS^{-}/PAH^{+}/PSS^{-}/{PAH-CNT-$AuNP^{+}$/ HRP^{-}}$_m$/{PAH-CNT-$AuNP^{+}$/$ChOx^{-}$}$_n$ [33].

Multilayer films of $PDDA^{+}$ wrapped CNT and two negatively-charged enzymes acyl-CoA synthetase (ACoAS) and acyl-CoA oxidase (ACoAOx) were assembled to obtain SPCE/{PDDA-CNT/ACoAOx}$_2$, or SPCE/{PDDA-CNT/ ACoAOx/PDDA-CNT/ACoAS}$_2$ [35].

Carboxylated-CNT were covalently bound to an Au electrode modified with either 11-amino-n-undecanethiol (AUT) or thionine via the Au-S bond to provide amino groups. Multilayer films of PAA^{+} and poly(vinyl sulfonate) (PVS^{-}), {PAA^{+}/PVS^{-}}$_3$/{$PDDA^{+}$/GOx^{-}}$_8$ were formed on Au/thionine^{+} /CNT^{-} or Au/AUT/CNT [34].

Carboxylated CNT were assembled together with PAMAM-NH_3^{+}-Au and the enzyme acetylcholine esterase ($AChE^{-}$) to obtain GCE/CNT^{-}/ PAMAM-NH_3^{+}-Au/$AChE^{-}$[32]. In [37], carboxylated CNT were functionalized with either PEI^{+}, DNA^{-}, or $AChE^{-}$, the latter being achieved with the aid of EDC/NHS, and self-assembled on GCE to obtain GCE/CNT-PEI^{+}/CNT-DNA^{-}/{CNT-PEI^{+}/CNT-$AChE^{-}$}$_3$ [36]. In a similar way, GCE/{CNT-PEI^{+}/CNT-DNA^{-}}$_2$ served as support for the deposition of organophosphate hydrolase (OPH^{+}) together with $AChE^{-}$ to obtain GC_2/OPH^{+}/$AChE^{-}$ [37].

A glucose biosensor was developed based on as-prepared PtNP-CNT^{-} composite and sugar-lectin biospecific interactions between concanavalin A (Con A) and GOx to obtain GCE/$chit^{+}$/PtNP-CNT^{-}/{Con A/GOx}$_3$[38].

3. ELECTROCHEMICAL AND SURFACE CHARACTERIZATION OF THE LBL MODIFIED ELECTRODES

3.1. Characterization by cyclic voltammetry

Cyclic voltammetry (CV) has often been employed to follow the deposition process of the multilayer composite films containing graphene and/or CNT. Unless the multilayers contained an electroactive component, $[Fe(CN)_6]^{4-/3-}$ was used as a redox probe to investigate the electrochemical properties of the modified electrodes.

3.1.1. Graphene modified electrodes

A Prussian blue (PB) containing multilayer deposited on GCE, GCE/{G/PDDA$^+$-PB/GOx$^-$/PDDA$^+$-PB}$_3$, exhibited a pair of redox peaks at 0.2 V *vs*. SCE in PBS pH 7.4, which corresponds to the redox conversion between PB and its reduced form, Prussian white (PW). The electrochemical properties of PB were not changed in the multilayer films and the redox peak currents increased with increasing number of bilayers [14]. Similarly, CVs confirmed the effective formation of the PB layer within the multilayer structure, based on octadecylamine (ODA) assembly to form SPE/ODA-G/ODA/PB, seen by the appearance of a well-defined pair of peaks with mid-point potential E_m = 0.19 V *vs*. Ag/AgCl, attributed to PB. The high peak-to-peak separation (100 mV) was due to mixed charge transfer and mass transport-limited process, attributed to the surface confined PB redox process and the physical transport of K^+ ions [27].

CVs of GCE/PDDA$^+$/{G$^-$/MG$^+$}$_n$ showed two pairs of peaks with E_m values of -0.13 V and -0.25 V *vs*. Ag/AgCl, the redox process being diffusion-controlled. When MG was adsorbed on GCE/PDDA$^+$/{G$^-$/CNT$^+$}$_5$, the redox peaks were located at -0.08 and -0.17 V *vs.* Ag/AgCl, and the process was surface-confined. The difference is explained considering the pH-dependent redox process of MG since, when MG is in multilayer structures, the diffusion of H^+ within the multilayers controls the redox process whilst when MG is adsorbed on the outer surface, H^+ in the buffer solution can easily participate in the redox process of MG and, so that the redox is surface-controlled. The high stability of the modified electrode was demonstrated by continuously cycling the electrode, the peak currents remaining constant after 50 cycles [16]. In [26], another phenazine monomer, methylene blue (MB), was used together with graphene in multilayer structures. In this case the electrode GCE/{G/MB}$_n$ displayed a pair of redox peaks with E_m = -0.25 V *vs.* SCE, corresponding to MB redox activity, which increased with the number of layers, reflecting the loading of MB and G in each layer onto GCE [26].

When G was acidically functionalized, well-defined peaks with E_m = 0.09 V *vs.* SCE observed for the Gr/PDDA$^+$/PSS$^-$/{CNT-NH$_3^+$/G-COO$^-$}$_5$, were attributed to the redox process of oxygen-containing groups, which increased linearly with the number of bilayers. The CV profile remained unaltered on continuous potential cycling, indicating the robustness of the multilayer film [15].

The deposition of {chit$^+$(CN+GOx)/PSS$^-$}$_n$ structures was monitored through the variation in the capacitance values calculated from the CVs. In [22], the deposition of first layer of chit$^+$(NG+GOx) led to a substantial increase in the capacitance value, decreasing when the second chit layer was adsorbed. In [23], the chitosan concentration was decreased to 0.5% compared to the 1% used in [22], due to the resistive nature of chitosan, but when the chitosan membrane contained HNO_3 or KOH functionalized CNT, the capacitance increased gradually up to the fourth chit layer. Highest capacitance values were recorded for electrode assemblies containing HNO_3_CNT and KOH_G, confirmed by electrochemical impedance spectroscopy measurements. CVs recorded without CN in the chitosan layer, revealed a continuous decrease in the capacitive currents upon chitosan deposition, underlying their importance.

The electrochemical properties of the multilayer film GCE/{PEI$^+$ /PAA$^-$}$_3$, with and without G, were assessed by using $[Fe(CN)_6]^{4-/3-}$ as electrochemical probe. Without graphene, the peak currents of the redox probe were smaller at the modified electrodes, and peak separation increased, indicating that the probe was hindered from permeating through the multilayer film and undergoing electron transfer at the electrode substrate. For the GCE/{PEI$^+$/PSS-G$^-$}$_3$ modified electrode, the CV response was nearly the same as that of the bare GC electrode, indicating that graphene can promote electron transfer through the multilayer film [17].

In a similar way, graphene promoted electron transfer through the multilayer film at GCE/ABS$^-$/{G-AB$^+$/G-TSCuPc$^-$}$_3$/G-AB$^+$, when graphene was functionalized prior to LbL assembly with either AB$^+$ or TSCuPc$^-$. The peak-to-peak separation of $[Fe(CN)_6]^{4-/3-}$ increased almost by a factor of 3 when GCE was modified with ABS$^-$, attributed to the presence of negatively-charged sulfonate groups on the surface, while upon inclusion of G as G-AB$^+$ and G-TsCuPC$^-$ in the multilayer, the reversibility was significantly reduced, and peak currents were enhanced [20]. Modification with {BSA-G$^+$/AuNP$^-$} led to an increase in the electroactive area, as measured using $[Fe(CN)_6]^{4-/3-}$. Moreover, annealed modified electrodes showed a higher electroactive area than non-annealed electrodes, due to an increase in film porosity; however, for annealing temperatures higher than 340ºC, the peak currents decreased, probably due to the partial decomposition of graphene [24]. Using chitosan matrices, an increase in the electroactive area, from 0.08 for GCE to 0.12 cm^2 GCE/{chit$^+$/G$^-$}$_5$, using $[Fe(CN)_6]^{4-/3-}$, was observed, indicating high conductivity of the multilayer films [25].

Successful attachment of pyrene-functionalized GOx was demonstrated by CV, the monolayer modified electrode presenting a redox peak at -50 mV *vs*. Ag/AgCl, related to GOx redox activity. $[Fe(CN)_6]^{4-/3-}$ redox peaks were significantly decreased in height after immobilization of graphene together with pyrene functionalized GOx due to the hindered access of the redox probe [21].

3.1.2. CNT modified electrodes

The deposition of PVI-Os^+ polymer in a multilayer structure with GOx-CNT^- was monitored by CV in phosphate buffer saline, pH 7.0. A pair of well-defined peaks with E_m = 0.23 V *vs*. Ag/AgCl was observed after the assembly of the first bilayer, ascribed to the PVI-Os groups' activity, which increased with the number of bilayers, suggesting an increase in the amount of electroactive PVI-Os immobilized on the electrode surface. Above 5 bilayers, the conductivity of the multilayer decreased, due to incorporated GOx hindering electron transfer through the film. The robustness of the SPCE/PVI-Os^+_{el}/{GOx-CNT^-/PVI-Os^+}$_4$/PVI-Os_{el}^+ modified electrode was confirmed by the stable CV profile upon potential cycling [29].

Similarly, the Os redox peaks which were observed for the first GOx/ SWCNT/PVI-Os layer assembled, increased with the number of GOx/SWCNT/ PVI-Os layers, suggesting an increase in Os complex content. However, the peak to peak separation increased due to the slower charge transfer displayed by PVI-Os. The electrochemical process was diffusion-controlled at both SPCE/PVI-Os^+_{el}/{GOx-CNT^-/PVI-Os^+}$_4$/PVI-Os_{el}^+ and SPCE/{PVI-Os^+_{el}/CNT^-/ PVI-Os_{el}/ GOx^-}$_5$/PVI-Os_{el}, being related to electron transfer in the redox polymer [30].

CNT^- deposition on GCE^+ led to an increase in the peak currents of $[Fe(CN)_6]^{4-/3-}$ and a decrease in the peak potential separation (ΔE_p). Moreover, due to the deposited positively-charged PEI^+, the peak currents increased more at GCE/CNT^-/PEI^+, due to more $[Fe(CN)_6]^{4-/3-}$ being adsorbed onto the positively charged PEI^+. Deposition of GOx led to a decrease in peak currents and an increase in ΔE_p as expected, indicative of the fact that GOx was immobilized successfully in the GCE/CNT^-/{PEI^+/GOx^-}$_3$ multilayer film [28].

CVs of the GCE/$chit^+$/PtNP-CNT^-/{Con A/GOx}$_3$ electrode, where Con A is concanavalin A, exhibited a pair of well-defined and stable redox peaks with E_m −0.42 V vs. SCE, with ΔE_p = 60 mV, attributed to the quasi-reversible redox reaction of GOx. The value of ΔE_p increased with increase in the number of layers, due to slower electron transfer kinetics. The electrochemical process was surface-confined up to 120 mV s^{-1}, above which it was diffusion-controlled [38]. In another PtNP containing multilayer deposited on ITO,

ITO/CNT$^-$/{PtNP-PAMAM$^+$/GOx$^-$}$_n$, the oxidation peak at −0.2 V *vs*. Ag/AgCl was ascribed to Pt redox activity and increased gradually with the number of deposited layers, up to 3 bilayers, after which the current tended to decrease gradually. The electrochemical oxidation of glucose was a diffusion-controlled process at the surface of the modified electrode [31].

The electrochemical performance of Au/thionine$^+$/CNT$^-$/{PAA$^+$/PVS$^-$}$_3$ was improved by replacing 11-amino-n-undecanethiol (AUT) with thionine to perpendicularly immobilize CNT on the Au surface, demonstrated by the increase in peak current of $[Fe(CN)_6]^{4-/3-}$. Au/AUT gave zero response and the calculated electroactive surface areas of Au/thionine$^+$, Au/AUT$^+$/CNT$^-$ and Au/thionine$^+$/CNT$^-$ were, respectively, 1.1, 1.0 and 1.2 that of the unmodified Au electrode, indicating that the insulating AUT layer completely blocked electron transfer, while thionine can increase the electron exchange between the Au electrode and the redox probe [34].

The peak current of the redox probe increased and ΔE_p decreased in the order GCE, GCE/{CNT-PEI$^+$/CNT-DNA$^-$}$_2$ and GCE/{CNT-PEI$^+$/CNT-DNA$^-$}$_2$/OPH$^+$/AChE$^-$. The electroactive area followed the same tendency, increasing from 0.06 cm^2, for the GCE, to 0.08 cm^2 and 0.12 cm^2. The electrochemical process was found to be diffusion-controlled. The six layered enzyme/polymer nanocomposite was found to have the highest surface area [37].

3.2. Surface characterization by AFM, SEM and TEM

3.2.1. Atomic force microscopy (AFM)

3.2.1.1. Graphene

AFM images of graphene-containing LbL-modified electrodes enabled the thickness of graphene oxide and of reduced graphene to be estimated in some cases. Usually, the deposition of LbL was monitored *via* the change in the surface roughness.

In [17], the thickness of graphene oxide was estimated to be 0.9 nm from AFM images, being larger for PAA-graphene in {PEI$^+$/PAA$^-$-G}, of 1.8 nm. Since the thickness of graphene is assumed to be less than that of graphene oxide, the thicker PAA-G indicates that PAA-pyrene is attached to graphene sheets, to obtain PAA$^-$-G. Similarly, in [18], the thickness of graphene oxide was about 0.95 nm, and the larger thickness of 1.36 and 1.59 nm for G-SO_3^- and G-IL-NH_3 was verification of the successful functionalization of G. The typical crumpled thin flake shape of GO is maintained after its functionalization [18]. AFM images show that BSA-G nanosheets were rougher and thicker than pristine GO indicating successful reduction and modification by BSA [24]. In [21], the graphene sheets in

{G/GOx-pyrene} were found to be mostly single-layered with an average size of about 300 nm.

AFM images of {G/PDDA$^+$-PB} multilayer films revealed a flat and homogeneous surface, in which the presence of both PB particles and graphene sheets are clear [14].

3.2.1.2. CNT

CNT networks can be more easily seen by AFM imaging, than those of graphene. It was observed that CNT form a monolayer of densely-packed bundles on Au/11-amino-n-undecanethiol (AUT) and Au/thionine, being perpendicularly fixed on both substrates. The similar densities observed confirmed that thionine can substitute AUT in the CNT assembly and the low average lateral dimensions of CNT of about 70 nm, indicate insignificant aggregation during CNT surface condensation [34]. In the CNT-PEI$^+$/CNT-DNA$^-$/{CNT-PEI$^+$/CNT-AChE$^-$} layers, bio-functionalized CNT, CNT-DNA$^-$ and CNT-AChE$^-$, form an interlocked network structure, the surface roughness increasing with the number of deposited layers, due to increased film thickness [36].

3.2.2. Scanning and transmission electron microscopy (SEM and TEM)

3.2.2.1. Graphene

SEM imaging revealed the shape of wrinkled graphene sheets, typical of exfoliated sheets of graphene, which is usually maintained even after its functionalization, as exemplified in Fig. 3a.

SEM images of both $\{G^-/CNT^+\}_n$ and $\{G^-/MG^+\}_n$, with methylene green, reveal an increase in surface coverage with the number of bilayers. In the case of $\{G^-/CNT^+\}_n$ the typical crumpled graphene structures were interconnected with the nanowire structures of CNT and form a network with large surface area. The same graphene structures were observed for $\{G^-/MG^+\}_n$ which were well interconnected to each other at the edges forming a well-structured conducting graphene/MG network [16]. The graphene crumpled sheet structures are visible in the SEM images of GCE/$\{chit^+/G^-\}_n$, and ITO/ (chit(G+GOx) [23] with a denser and more uniform surface with deposition of more bilayers [25].

The morphologies of G-SO_3^- and G-IL-NH_3^+ used in {G-IL-NH_3^+/G-SO_3^-} multilayers are different. The G-SO_3^- is not greatly changed compared to G, while the G-IL-NH_3^+ has a different aspect to that of G, appearing to be covered by a thin layer of IL. The first monolayer did not cover the ITO surface completely with G, but with an increasing number of bilayers, the graphene gradually

builds up and is densely assembled up to the 5th bilayer [18]. Similar structures of wrinkled graphene sheets were observed for both G-AB^{+} and G-TSCuPc^{-}, which retained the initial shape of G. The EDS spectra of the composites confirmed the presence of AB, by Cu and Cl signals and the Cu, O and S signals proved the presence of TSCuPc, after 3 layers the substrate being densely covered by graphene [20].

In the case of G-TiO_2-Pd^{-} used in the {CNT-NH_3^{+}/G-TiO_2-Pd^{-}}$_9$ multilayer film, SEM images of graphene without any particle loading revealed thicker platelets with multiple layers of graphene sheets, indicating that the exfoliated parts restacked together due to capillary and van der Waals forces. After reacting with $TiCl_3$, the multi-layered graphene sheets are entirely covered by TiO_2, which form distinct irregular spherical and rod-like morphologies, while the wrinkle structure of graphene is maintained. Elemental analyses further attest the presence of Ti on graphene surfaces. TEM images of G-TiO_2-Pd^{-} show uniformly distributed small PdNP on top of G-TiO_2 with no agglomeration and with an average nanorod diameter of 7–10 nm and length 40–60 nm. The average size of the deposited PdNPs is 5.5±0.3 nm [19].

SEM images of graphene/AuNP hybrid multilayer films, FTO/PEI/{BSA-G^{+}/AuNP^{-}}, showed that AuNPs were uniformly distributed on the surface of the graphene nanosheets. Side-view SEM images illustrated that the AuNPs were LbL-stacked, the film thickness increasing linearly with the number of bilayers [24].

Finally, SEM images obtained during the LbL modification of graphite substrate showed that the cavities observed at the bare graphite electrode, decreased upon modification with the first CNT-NH_3^{+}/G-COO^{-} bilayer, more G and CNT being adsorbed in the following bilayers [15].

3.2.2.2. CNT

SEM images of CNT within the LBL multilayers usually reveal their typical nanotube, three-dimensional structures (see Fig. 3b). As in the case of graphene, typically more than 2-3 bilayers are needed to completely cover the substrate surface.

An increase in CNT surface thickness demonstrates the effectiveness of the LbL process, when bio-functionalized CNTs, CNT-DNA^{-} and CNT-AChE^{-}, are randomly dispersed in the thin films of CNT-PEI^{+}/CNT-DNA^{-}/{CNT-PEI^{+}/CNT-AChE^{-}}$_3$ [36].

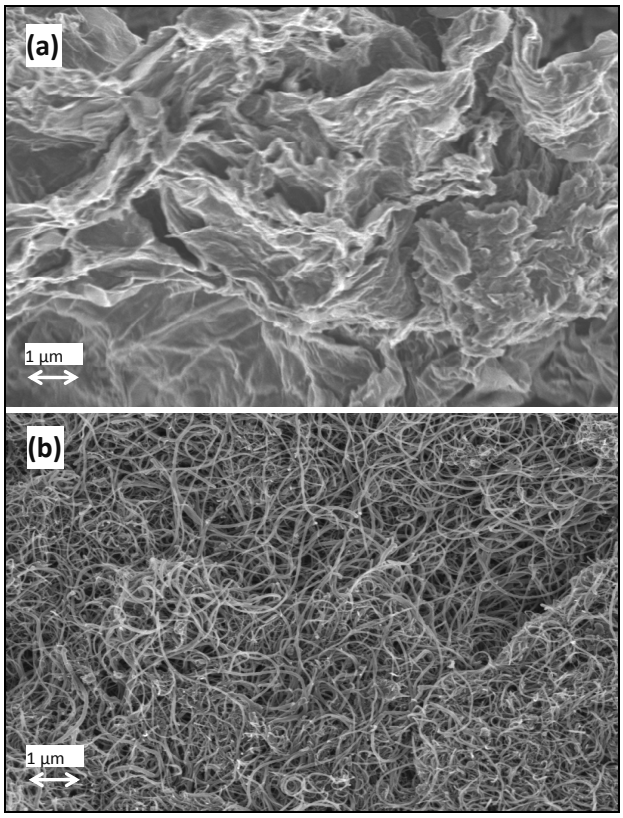

Figure 3. Typical SEM images of a) G and b) CNT on indium tin oxide substrates

CNT were efficiently covered by the PEI^+ polymeric net in GCE/CNT^-/PEI^+ and were homogenously distributed on the GCE surface. GOx molecules adsorbed on the surface of GCE/CNT^-/PEI^+ tended to aggregate into island-like structures. In GCE/CNT^-/{PEI^+/GOx^-}$_3$/PEI^+, CNT are hardly visualized, being totally wrapped by both protein and PEI polymer [28]. In the case of SPCE/{PVI-Os^+_{el}/CNT^-/PVI-Os_{el}/GOx^-}$_5$/PVI-Os_{el} SEM images show that the substrate is almost completely covered with a homogeneous, porous, three-dimensional CNT-polymer nanocomposite [30].

Typical SEM images of CNT dispersed in chitosan clearly reveal the CNT tubular structure with a more curved and less aligned arrangement, with no sign of residual metal particles. The images showed nanotubes with diameters between 20 and 44 nm, which correspond with the initial values after fabrication (30±10 nm), which indicates that their functionalization does not modify their initial structure [23].

TEM images at LbL modified electrodes containing PtNP and CNT show that PtNP are highly dispersed and distributed either on the sidewall, in chit$^+$/PtNP-CNT$^-$ [38], or on the surface of CNT, in CNT$^-$/Pt-PAMAM$^+$ [31], in the latter case the dendrimer acting as a stabilizer, by impeding the regrouping of nanoparticles. Also, when AuNP were used together with CNT, they were uniformly dispersed without aggregation on the CNT surface, which were randomly oriented and distributed in the PAH-CNT-AuNP layer without aggregation. Up to 4 layers, the surface was not fully covered, while eight layers ensured a high surface coverage [33]. SEM images confirmed the presence of some free AuNP and intra-PAMAM dendrimer AuNP nanostructures, with 13 nm diameter, with the size of the AuNPs inside being of 8 nm [32].

4. APPLICATIONS

The majority of the biosensors developed in the past 5 years based on LbL methodology have been glucose biosensors utilizing GOx, some others containing the enzymes AlcDH, ChOx, acyl-CoA oxidase/ synthetase. Three biosensors were based on enzyme inhibition and two were developed to be used in biofuel cells.

Table 1 summarises the biosensors that have been developed and their principal analytical characteristics.

Table 1. Biosensors based on carbon nanomaterials, graphene and CNT, and LbL methodology from 2010-2015

Analyte	Electrode architecture	Technique	Linear range / mM	LOD / µM	Sensitivity / µA mM^{-1} cm^{-2}	Ref.
Glucose	GCE/{G/PDDA$^+$-PB/GOx$^-$/ PDDA$^+$-PB}$_3$	Amp. +0.2 V$^{(b)}$	0.1-6.5	6	1.6*	[14]
	GCE/{PEI$^+$/PAA$^-$-G}$_3$/ {PEI$^+$/GOx$^-$}$_5$	Amp. +0.9 V	0.2-10	168	0.261	[17]
	GCE/{G/GOx-pyrene}$_3$	Amp. +0.28 V$^{(a)}$	0.2-30	154	2.0	[21]
	GCE/{G-IL-NH$_3^+$/G-SO$_3^-$}$_5$/ G-IL-NH$_3^+$/GOx$^-$/Nafion	Amp. -0.2 V	0.01-0.5	3.3	1	[18]
	GCE/ABS$^-$/{G-AB$^+$/ G-TSCuPc$^-$}$_3$/G-AB$^+$/Nafion/GOx	CV-0.45 V$^{(b)}$	0.1-8.0	50	17.5	[20]
	AuQC/{chit$^+$(HNO$_3$_G+GOx)/ PSS$^-$}$_4$ AuQC/{chit$^+$(KOH_G+GOx)/ PSS$^-$}$_4$	Amp -0.3 V$^{(a)}$	0.2-1.6 0.2-1.6	64 12	6.0 18.6	[23]
	AuQC/{chit$^+$(NG+GOx)/PSS$^-$}$_2$	Amp. -0.2 V$^{(a)}$	0.2-1.6	18.6	10.5	[22]

Analyte	Electrode architecture	Technique	Linear range / mM	LOD / µM	Sensitivity / µA mM^{-1} cm^{-2}	Ref.
	GCE/{CNT-NH_3^+/G-TiO_2-PdNP$^-$}$_9$/ CNT-NH_3^+/GOx$^-$/Nafion	Amp. -0.05 V[(b)]	0.001-1.5	0.6	0.18	[19]
	AuQC/{chit$^+$(HNO_3_CNT+GOx)/ PSS^-}$_4$ AuQC/{chit$^+$(KOH_CNT+GOx)/ PSS^-}$_4$	Amp. -0.3 V[(a)]	0.2-1.6 0.2-1.6	18 50	18.6 13.7	[23]
	GCE/CNT$^-$/{PEI$^+$/GOx$^-$}$_3$/PEI$^+$	CV -0.5 V[(b)]	0.3	-	106.6	[28]
	SPCE/PVI-Os^+_{el}/{GOx-CNT$^-$/ PVI-Os^+}$_4$/PVI-Os_{el}^+	Amp. +0.3 V[(a)]	0.2-7.5	0.07	32	[29]
	SPCE/{PVI-Os^+_{el}/CNT$^-$/ PVI-Os_{el}/ GOx$^-$}$_5$/PVI-Os_{el}	Amp. +0.3 V[(a)]	0.2-6.0	100	16.4	[30]
	GCE/chit$^+$/PtNP-CNT$^-$/ {Con A/GOx}$_3$	Amp. +0.3 V[(b)]	0.001-2.0	0.4	41.9	[38]
	Au/thionine$^+$/CNT$^-$/ {PAA^+/PVS^-}$_3$/{PDDA$^+$/GOx$^-$}$_8$	Amp. +0.6 V[(a)]	0.05-6.3	11	19	[34]
Maltose	GCE/{PEI$^+$/PAA$^-$-G}$_3$/ {PEI$^+$/GOx$^-$}$_5$/{PEI/GA}$_4$	Amp. +0.9 V	10-100	1370	0.00715	[17]
Ethanol	Gr/PDDA$^+$/PSS$^-$/{CNT-NH_3^+/ G-COO^-}$_5$/AlcDH.	Amp. +0.1 V[(b)]	0.025-0.2	25	82.5	[15]
	GCE/PDDA$^+$/{G$^-$/MG$^+$}$_5$/AlcDH	Amp. +0.1 V[(a)]	0.5-11.0	-	0.025	[16]
Cholesterol	Au/MPS$^-$/PAH$^+$/PSS$^-$/ {PAH-CNT-AuNP/HRP)$_m$/ {PAH-CNT-AuNP/ChOx}$_n$	Amp. -0.15 V[(b)]	0.18-11	20	0.12	[33]
Palmitoyl-CoA Oleic acid	SPCE/{PDDA-CNT/ACoAOx}$_2$ SPCE/{PDDA-CNT/ACoAOx/ PDA-CNT/ACoAS}$_2$	LSV +0.5 V[(c)]	up to 1.2 up to 0.9	- -	8.9 12.3	[35]

* Area not specified; [(a)] *vs*. Ag/AgCl, [(b)] *vs*. SCE; [(c)] Ag

G - graphite, **PDDA** - poly(dimethyldiallyammonium chloride), **PB** - Prussian blue nanoparticles; **GOx** – glucose oxidase; **PEI** - polyethyleneimine, **PAA** -polyallylamine, **IL**-ionic liquid, **ABS**$^-$ - sulfanilic acid, **AB** - alcian blue pyridine variant, **TSCuPc** - copper phthalocyanine-tetrasulfonic acid tetrasodium salt, **PSS** -poly(sodium-p-styrene-sulfonate), **chit** – chitosan, **NG**- nitrogen doped graphene, **PdNP** – Pd nanoparticles, **SPCE** - screen printed carbon electrode, **PVI-Os**-(poly[(vinylpyridine) Os(bipyridyl)$_2$Cl, **PVI-Os$_{el}$** – PVI-Os electrodeposited, **PtNP**- Pt nanoparticles, **Con A**- concanavalin A, **PVS** - poly(vinyl sulfate), **GA-** glucoamylase, **AlcDH** –alcohol dehydrogenase, **MG** – methylene green, **MPS**- 3-mercapto-1-propanesulfonate, **PAH** - poly(allylamine hydrochloride), **AuNP**- Au nanoparticles, **HRP** – horseradish peroxidase, **ChOx** – cholesterol oxidase, **ACoAOx** -acyl-CoA oxidase, **ACoAS** acyl-CoA synthetase.

4.1. Glucose biosensors

Glucose oxidase (GOx) has several favourable attributes that contribute to its common usage such as high turnover rate, excellent selectivity, good thermal and pH stability, and low cost and robustness [39-41]. Hence, GOx based biosensors are continuously developed, serving usually as a strategy to evaluate new electrode biosensor platforms. Glucose biosensors have been developed based on the LbL methodology and will be briefly described in this section.

The glucose biosensors developed were based on H_2O_2 detection [14, 17-19, 34], or direct electronic communication between the enzyme and the electrode [20, 22, 23, 28, 38], only few utilizing a redox mediator [21, 29, 30].

In [14], the use of PB, which has been demonstrated to have intrinsic peroxidase activity, allowed glucose monitoring through detection of H_2O_2 at +0.20 V *vs*. SCE. Also on the basis of the high electrocatalytic activity of GCE/{PEI^+/PAA^--G}$_6$ toward H_2O_2, glucose and maltose enzyme-based biosensors were fabricated, incorporating GOx together with glucoamylase (GA) [17]. Similarly, GCE/{G-IL-NH_3^+/G-SO_3^-}[18], GCE/{CNT-NH_3^+/G-TiO_2-$PdNP^-$}$_n$ [19] and Au/thionine$^+$/CNT^-/{PAA^+/PVS^-}$_3$, [34] showed a similar electrocatalytic effect towards H_2O_2, the measurement of glucose being based on H_2O_2 detection.

Graphene used in GCE/ABS^-/{G-AB^+/G-$TSCuPc^-$}$_3$/G-AB^+/Nafion/GOx enabled direct electron transfer between the redox centres of GOx molecules and the electrode substrate, the glucose being detected by monitoring the GOx peaks in CV. The mechanism was based on the gradual decrease of the reduction peaks, due to O_2 consumption upon addition of glucose [20].

Biosensors based on carbon nanomaterials (CN) in the configuration {$chit^+$(CN+GOx)/PSS^-}$_n$, n = 2, where CN = nitrogen-doped graphene (NG) and n = 4 when CN = HNO_3 or KOH functionalized G and CNT, showed good electronic communication between GOx and the electrode substrate *via* G or CNT. The mechanism was based on direct cofactor regeneration at the electrode at -0.3 and -0.2 V *vs.* Ag/AgCl. The biosensor architectures with best sensitivities and stability were based on four bilayers, the sensitivity being greatly influenced by the capacitance of the modified electrodes [22, 23].

In the case of the GCE/CNT^-/{PEI^+/GOx^-}$_3$/PEI^+ biosensor, it was demonstrated that CNT play a critical role in the direct electron transfer of GOx, their presence leading to a significant increase of the GOx redox peaks. The CV peak currents also increased linearly with the number of bilayers up to the third, no increase being observed on depositing more bilayers. The midpoint potential of GOx was -0.45 V, very close to the standard $FAD/FADH_2$ potential of −0.46 V *vs*. SCE at pH 7.0, 25 ◦C [42], indicating that most GOx molecules retain their native structure after immobilization. Moreover, the peak-to-peak separation was only 40 mV, indicating fast electron transfer [28].

Similar to the biosensor developed in [28], the GCE/chit^{+}/PtNP-CNT^{-}/{Con A/GOx}$_3$ biosensor was based on direct electron transfer, the CV displaying a pair of peaks around -0.45 V, again close to the standard FAD/$FADH_2$ potential. PtNP play a dual role, as immobilization matrices for the enzyme and as electrocatalytic material for glucose oxidation, at +0.3 V *vs*. SCE [38].

In [21], the LbL assembly was based on π-π interaction between pyrene-functionalized GOx and graphene; therefore, the enzymatic activity of GOx-pyrene was first assessed, results indicating retention of 76% of its biocatalytic activity. Ferrocene was used to mediate electrical communication between the enzyme and the electrode.

SPCE/PVI-Os$^{+}_{el}$/{GOx-CNT^{-}/PVI-Os^{+}}$_n$ and SPCE/{PVI-Os$^{+}_{el}$/CNT^{-}/PVI-Os$_{el}$/GOx^{-}}$_n$/PVI-Os$_{el}$ biosensors were based on oxidation of the mediator at +0.3 V *vs*. Ag/AgCl [29, 30]. The currents increased linearly up to 4 and 5 bilayers respectively, further bilayers tending to gradually decrease the catalytic current, due to hindered glucose transport through the multilayers.

Negligible or no interferences were observed from ascorbic acid (AA), uric acid (UA) and dopamine (DA) [14, 18-23, 34] nor acetaminophen [29, 34], H_2O_2 and L-cysteine [20], or citric and oxalic acid [22, 23]. UA and AA greatly influenced biosensor response in [29], their pre-oxidation being required before the use of the biosensor for glucose detection in complex matrices. In [30], the authors decreased the interferences by using a Nafion membrane as an outer negative layer,

Biosensors retained 83% [18], 86% [19] and 90% [34] of their initial activities after two weeks of storage at 4 ºC. Biosensor response decreased by only 7% [20], 10 % [29, 30] and 18% [21] after one month of storage at 4 ºC. The current recorded at GCE/CNT^{-}/{PEI^{+}/GOx^{-}}$_3$/PEI^{+} decreased by 5% after storage at 4 ºC for 20 days[28] and the biosensor current response in CV decreased by 5.6% in 10 days, and by 13% after 1 month of storage [38]. In most of these reports, the storage medium (air or buffer solution) is not specified, only the temperature.

After 10 days of continuous use, sensitivities decreased by 10 % for HNO_3_CNT and KOH_G biosensors, and 5 % for KOH_CNT and HNO_3_G biosensors, respectively. After 20 days the sensitivities maintained 70 %, for HNO_3_CNT and KOH_G biosensors, and 60% of their initial values for KOH_CNT and HNO_3_G biosensors. The biosensor based on NG maintained 95 % of its initial sensitivity after two weeks of continuous use [22, 23].

4.2. Biosensors for ethanol, cholesterol and fatty acids

Two biosensors for the determination of ethanol were developed, both based on alcohol dehydrogenase (AlcDH), one containing both CNT and G, Gr/PDDA^{+}/PSS^{-}/{CNT-NH_3^{+}/G-COO^{-}}$_5$/AlcDH [15] and one comprising the redox mediator methylene green (MG) and G, GCE/PDDA^{+}/{G^{-}/MG^{+}}$_5$/AlcDH [16].

The oxidation of NADH was first tested at Gr/PDDA^{+}/PSS^{-}/{CNT-NH_3^{+}/G-COO^{-}}$_5$ at +0.07 V *vs*. SCE, no significant interferences being observed from UA, DA, acetaminophen and H_2O_2. The biosensor operated at +0.10 V *vs.* SCE and the mechanism was based on the oxidation of the cofactor. After 5 days, the biosensor retained 92% of the initial response [15].

The assembled GCE/PDDA^{+}/{G^{-}/MG^{+}}$_5$ possessed electrocatalytic activity toward the oxidation of NADH, which occurred at -0.10 V *vs*. Ag/AgCl. The AlcDH biosensor operated at +0.10 V, the mechanism being based on cofactor regeneration [16].

A bi-enzymatic biosensor based on horseradish peroxidase (HRP) and cholesterol oxidase (ChOx) was developed for the detection of cholesterol. The mechanism of Au/MPS^{-}/PAH^{+}/PSS^{-}/{PAH-CNT-AuNP/HRP)$_m$ /{PAH-CNT-AuNP/ChOx}$_n$ was based on the amperometric detection of H_2O_2 at -0.15 V *vs*. SCE, a by-product of the enzymatic conversion of cholesterol in the presence of oxygen. The biosensor could detect cholesterol without HRP at -0.15 V, due to the catalytic properties of AuNP and CNT, but the presence of HRP significantly increased the sensitivity. No significant interferences were observed from urea, glycine, l-cysteine, glucose and AA. After 25 days of storage the biosensor maintained 90% of its initial response. The biosensor was successfully applied to the detection of cholesterol in human serum samples [33].

An acyl-CoA oxidase (ACoAOx) biosensor, SPCE/{PDDA-CNT/ACoAOx}$_2$, was developed for the detection of palmitoyl oil and a bi-enzymatic biosensor based on ACoAOx together with acyl-CoA synthetase (ACoAS), SPCE/{PDDA-CNT/ACoAOx/PDA-CNT/ACoAS}$_2$, for the determination of oleic acid. The detection of both oleic acid and palmitoyl-CoA was based on the oxidation of enzymatic generated H_2O_2 at +0.5 V *vs.* Ag. The bi-enzyme biosensor exhibited good electrocatalytic activity for oxidation of non-esterified fatty acids, the thin LbL polymer–enzyme layers allowing good reactant mass transport to accomplish the two-step enzyme reactions [35].

4.3. Biosensors based on inhibition

Three LbL biosensors based on acetylcholinesterase (AChE) inhibition were developed for the detection of pesticides and neurotoxins. The inhibition measurements for carbofuran were performed by differential pulse voltammetry at +0.63 V *vs.* SCE at GCE/CNT/PAMAM-NH_3^{+}-AuNP/AChE^{-}, and the sensor exhibited a detection limit of 4 nM, with a linear range 5-90 μM [32]. The inhibition by neurotoxins at GCE/CNT-PEI^{+}/CNT-DNA^{-}/{CNT-PEI^{+}/CNT-AChE^{-}}$_3$ was detected by fixed potential amperometry at +0.58 V *vs*. Ag/AgCl [36]. Organophosphorus and non-organophosphorus pesticides, namely paraoxon and carbaryl, were successfully detected by CV at +0.6 V *vs*. Ag/Agcl at a bi-enzymatic biosensor containing together with AChE the enzyme organophosphate

hydrolase (OPH), GCE/{CNT-PEI^{+}/CNT-DNA^{-}}$_2$/OPH^{+}/AChE^{-}. The detection limits were 0.5 and 1 μM for paraoxon and carbaryl respectively, the biosensors being successfully applied for detection of pesticides in apples [37].

4.4. Bioanodes for fuel cells

Three biosensors were developed for use as bioanodes in fuel cells, two based on GOx: ITO/CNT^{-}/{PtNP-PAMAM^{+}/GOx^{-}}$_3$ and ITO/CNT^{-}/{PDDA^{+}/GOx^{-}}$_3$ [31] and one on glucose dehydrogenase (GlcDh), GCE/PDDA^{+}/MG/{G^{-}/CNT^{+}}$_5$/ GlcDh [16]. In [31] the the ITO/CNT^{-}/{PtNP-PAMAM^{+}/GOx^{-}}$_3$ anode is coupled with a cathode consisting on electrodeposited Pt. Maximum power density and current density for ITO/CNT^{-}/{PDDA^{+}/GOx^{-}}$_3$ were 7 μW cm^{-2} and 75 μA cm^{-2}, respectively, while for (ITO/CNT^{-}/{PtNP-PAMAM^{+}/GOx^{-}}$_3$ the maximum power density was 17 μW cm^{-2} and current density was 90 μA cm^{-2}. Open circuit potentials were 0.52 V and 0.64 V, respectively. In [16], the anode GCE/PDDA^{+}/ MG/{G^{-}/CNT^{+}}$_5$/GlcDh was assembled with a laccase-based biocathode to form a glucose/O_2 biofuel cell, with an open circuit potential of 0.69 V and a maximum power density of 22.5 μW cm^{-2} at 0.48 V.

5. CONCLUSIONS

The use of LbL methodology incorporating graphene and carbon nanotubes in the modified electrode assemblies offers the possibility of developing a vast diversity of biosensor architectures, by exploiting different functionalizations of the carbon nanomaterials and choosing an appropriate polyelectrolyte for the build-up of the multilayers. The typical nanostructures of both graphene and CNT remain mostly unaltered after functionalization and self-assembly, their incorporation in the LbL structures leading to an overall increase in electronic conductivity and electroactive surface area of the modified electrodes which, as a result, improved the analytical performances of the LbL CN-based biosensors. During the time period reviewed, the majority of the LbL CN biosensors developed were based on glucose oxidase. Other biosensors were based on cholesterol oxidase, alcohol dehydrogenase, acyl-CoA oxidase/synthetase for the detection of ethanol, cholesterol and fatty acids, respectively. Biosensors based on the inhibition of acetylcholinesterase for the detection of neurotoxins and pesticides and three bioanodes were also reported using the enzymes glucose oxidase and glucose dehydrogenase.

Future research in this area should bring valuable contributions for the development of advanced LbL biosensors containing a variety of materials tailored in self-assembled thin multilayers, which can find applications in a variety of fields, such as clinical, food/environmental industry, and including the design of new bioanodes for fuel cells.

ACKNOWLEDGEMENTS

Financial support from Fundação para a Ciência e a Tecnologia (FCT), Portugal PTDC/QUI-QUI/116091/2009, POCH, POFC-QREN (co-financed by FSE and European Community FEDER funds through the program COMPETE and FCT project PEst-C/EME/UI0285/2013) is gratefully acknowledged. M.M.B. thanks FCT for postdoctoral fellowship SFRH/ BPD/72656/2010.

REFERENCES

1. L. Caseli, D.S. dos Santos Jr., R.F. Aroca, O.N. Oliveira Jr., *Material Science & Engineering C*, **2009**, *29*, 1687.
2. L. Caseli, D.S. dos Santos Jr., M. Foschini, D. Goncalves, O.N. Oliveira Jr., *Material Science and Engineering C*, **2007**, *27*, 1108.
3. R.M. Iost, F.N. Crespilho, *Biosensensor & Bioelectronics*, **2012**, *31*, 1.
4. O.N. Oliveira, R.M. Iost, J.R. Siqueira Jr., F.N. Crespilho, L. Caseli, *ACS Applied Materials & Interfaces*, **2014**, *6*, 14745.
5. V. Flexer, E.S. Forzani, E.J. Calvo, *Analytical Chemistry*, **2006**, *78*, 399.
6. S.M. Zhu, J.J. Guo, J.P. Dong, Z.W. Cui, T. Lu, C.L. Zhu, D. Zhang, J. Ma, *Ultrasonics Sonochemistry*, **2013**, *20*, 872.
7. Y. Shao, J. Wang, H. Wu, J. Liu, I.A. Aksay, Y. Lin, *Electroanalysis*, **2010**, *22*, 1027.
8. S.K. Vashist, D. Zheng, K. Al-Rubeaan, J.H.T. Luong, F.-S. Sheu, *Biotechnology Advances*, **2011**, *29*, 169.
9. T. Kuila, S. Bose, P. Khanra, A.K. Mishra, N.H. Kim, J.H. Lee, *Biosensors & Bioelectronics*, **2011**, *26*, 4637.
10. D. Tasis, N. Tagmatarchis, A. Bianco, M. Prato, *Chemical Reviews*, **2006**, *106*, 1105.
11. T. Kuila, S. Bose, A.K. Mishra, P. Khanra, N.H. Kim, J.H. Lee, *Progress in Materials Science*, **2012**, *57*, 1061.
12. V. Georgakilas, M. Otyepka, A.B. Bourlinos, V. Chandra, N. Kim, K.C. Kemp, P. Hobza, R. Zboril, K.S. Kim, *Chemical Reviews*, **2012**, *112*, 6156.
13. Q. He, Y. Cui, S. Ai, Y. Tian, J. Li, *Current Opinion in Colloid and Interface Science*, **2009**, *14*, 115.
14. J. Yan, T. Zhong, W. Qi, H. Wang, *Journal of Inorganic* and *Organometallic Polymers and Materials*, **2015,** *25*, 275.
15. S. Prasannakumar, R. Manjunatha, C. Nethravathi, G.S. Suresh, M. Rajamathi, T.V. Venkatesha, *Journal of Solid State Electrochemistry*, **2012**, *16*, 3189.
16. X. Wang, J. Wang, H. Cheng, P. Yu, J. Ye, L. Mao, *Langmuir*, **2011**, *27*, 11180.
17. G. Zeng, Y. Xing, J. Gao, Z. Wang, X. Zhang, *Langmuir*, **2010**, *26*, 15022.
18. H. Gu, Y. Yu, X. Liu, B. Ni, T. Zhou, G. Shi, *Biosensors & Bioelectronics*, **2012**, *32*, 118.
19. Y. Yu, Y. Yang, H. Gu, D. Yu, G. Shi, *Analytical Methods*, **2013**, *5*, 7049.

20. Y.-Q. Zhang, Y.-J. Fan, L. Cheng, L.-L. Fan, Z.-Y. Wang, J.-P. Zhong, L.-N. Wu, X.-C. Shen, Z.-J. Shi, *Electrochimica Acta*, **2013**, *104*, 178.
21. J. Liu, N. Kong, A. Li, X. Luo, L. Cui, R. Wang, S. Feng, *Analyst*, **2013**, *138*, 2567.
22. M.M. Barsan, M. David, M. Florescu, L. Ţugulea, C.M.A. Brett, *Bioelectrochemistry*, **2014**, *99*, 46.
23. M. David, M.M. Barsan, M. Florescu, C.M.A. Brett, *Electroanalysis*, **2015,** in press.
24. Q. Xi, X. Chen, D.G. Evans, W. Yang, *Langmuir*, **2012**, *28*, 9885.
25. X. Weng, Q. Cao, L. Liang, J. Chen, C. You, Y. Ruan, H. Lin, L. Wu, *Talanta*, **2013**, *117*, 359.
26. D. Zhang, L. Fu, L. Liao, B. Dai, R. Zou, C. Zhang, *Electrochimica Acta*, **2012**, *75*, 71.
27. A. Michopoulos, A. Kouloumpis, D. Gournis, M.I. Prodromidis, *Electrochimica Acta*, **2014**, *146*, 477.
28. C. Deng, J. Chen, Zhou Nie, S. Si, *Biosensors & Bioelectronics*, **2010**, *26*, 213.
29. Q. Gao, Y. Guo, W. Zhang, H. Qi, C. Zhang, *Sensors & Actuators B*, **2011**, *153*, 219.
30. Q. Gao, Y. Guo, J. Liu, X. Yuan, H. Qi, C. Zhang, *Bioelectrochemistry*, **2011**, *81*, 109.
31. J. Zhang, Y. Zhu, C. Chen, X. Yang, C. Li, *Particuology*, **2012**, *10*, 450.
32. Y. Qu, Q. Sun, F. Xiao, G. Shi, L. Jin, *Bioelectrochemistry*, **2010,** *77*, 139.
33. X. Cai, X. Gao, L. Wang, Q. Wu, X. Lin, *Sensors & Actuators B*, **2013**, *181*, 575.
34. M. Ma, Z. Miao, D. Zhang, X. Du, Y. Zhang, C. Zhang, J. Lin, Q. Chen, *Biosensors & Bioelectronics*, **2015**, *64*, 477.
35. J. Kang, A.T. Hussain, M. Catt, M. Trenell, B. Haggett, E.H. Yu, *Sensors & Actuators B*, **2014**, *190*, 535.
36. Y. Zhang, M.A. Arugula, J.S. Kirsch, X. Yang, E. Olsen, A.L. Simonian, *Langmuir*, **2015**, *31*, 1462.
37. Y. Zhang, M.A. Arugula, M. Wales, J. Wild, A.L. Simonian, *Biosensors & Bioelectronics*, **2015**, *67*, 287.
38. W. Li, R. Yuan, Y. Chai, H. Zhong, Y. Wang, *Electrochimica Acta*, **2011**, *56*, 4203.
39. R. Wilson, A.P.F. Turner, *Biosensors & Bioelectronics*, **1992**, *7*, 165.
40. J. Wang, *Chemical Reviews*, **2008**, *108*, 814.
41. N.S. Oliver, C. Toumazou, A.E.G. Cass, D.G. Johnston, *Diabetic Medicine*, **2009**, *26*, 197.
42. S. Q. Liu, H.X. Ju, *Biosensors & Bioelectronics*, **2003**, *19*, 177.